A New Preprocessing Technique for Fast Hyperspectral Endmember Extraction

Sebastian Lopez, *Member, IEEE*, Javier F. Moure, Antonio Plaza, *Senior Member, IEEE*, Gustavo M. Callico, *Member, IEEE*, Jose F. Lopez, and Roberto Sarmiento

***Abstract*—Hyperspectral image processing represents a valuable tool for remote sensing of the Earth. This fact has led to the inclusion of hyperspectral sensors in different airborne and satellite missions for Earth observation. However, one of the main drawbacks encountered when dealing with hyperspectral images is the huge amount of data to be processed, in particular, when advanced analysis techniques such as spectral unmixing are used. The main contribution of this letter is the introduction of a novel preprocessing (PP) module, called SE^{2}PP, which is based on the integration of spatial and spectral information. The proposed approach can be combined with existing algorithms for endmember extraction, reducing the computational complexity of those algorithms while providing similar figures of accuracy. The key idea behind SE^{2}PP is to identify and select a reduced set of pixels in the hyperspectral image, so that there is no need to process a large amount of them to get accurate spectral unmixing results. Compared to previous approaches based on similar spatial and spatial–spectral PP strategies, SE^{2}PP clearly outperforms their results in terms of accuracy and computation speed, as it is demonstrated with artificial and real hyperspectral images.**

***Index Terms*—Endmember extraction, hyperspectral imaging, linear spectral unmixing, NFINDR, orthogonal subspace projection (OSP), region-based spatial preprocessing (RBSPP), SPP, spatial–spectral PP (SSPP), vertex component analysis (VCA).**

I. Introduction

LINEAR spectral unmixing is a very important tool for analyzing the content of remotely sensed hyperspectral images [1]. It is based on the idea that each pixel vector $r = [r^1, r^2, \ldots, r^N]^{\mathrm{T}}$ in a hyperspectral image R composed by N spectral bands can be represented as a linear combination of p spectrally pure constituent spectra or endmembers e_i weighted by their corresponding abundance fractions a_i that quantify the proportion of each endmember in the pixel under inspection as follows:

$$\boldsymbol{r} = \sum_{i=1}^{p} \boldsymbol{a_i} \times \boldsymbol{e_i} + \boldsymbol{\varepsilon} \tag{1}$$

where ε represents a source of additive noise inherent to the sensing process. One of the most challenging tasks within the whole process of unmixing a hyperspectral image is the extraction of its endmembers. This is because of two main reasons. First, the extraction of a set of accurate endmembers is critical for the proper unmixing of the hyperspectral image under analysis. Second, the extraction process generally demands a formidable computational effort which becomes prohibitive for applications under real-time constraints.

In order to improve the performance of the aforementioned endmember extraction step, different algorithms that not only take into account the spectral characteristics of the hyperspectral image to be unmixed but also benefit from the inherent spatial correlation between pixels in spatially adjacent regions have been recently uncovered in the scientific literature. These algorithms can be classified into two groups. The first one is constituted by those approaches which incorporate the spatial information of the targeted image to the extraction process itself, such as the automatic morphological endmember extraction [2] and the spatial–spectral endmember extraction [3] approaches. The second group is composed by the algorithms in which the spatial information is exploited at a preprocessing (PP) stage that modifies the hyperspectral image prior to the extraction, such as the spatial PP (SPP) [4], the region-based SPP (RBSPP) [5], and the spatial–spectral PP (SSPP) [6] algorithms. As it can be noticed, the main difference between both groups is that, while the approaches categorized in the first one are endmember extraction algorithms themselves, the algorithms in the second group can be simply combined with existing extraction algorithms in order to compute the endmembers of an image. This introduces several advantages, including the fact that there is no need to modify the extraction algorithm in order to include spatial information.

More concretely, the RBSPP and the SSPP algorithms have demonstrated to offer not only proper levels of extraction accuracy but also a reduced computational cost when combined with classical endmember extraction algorithms. This is due to the fact that, prior to the extraction, both PP stages select a subset of pixels from the input image that are more likely to be the sought-after endmembers. However, these algorithms suffer, at least, from the following three drawbacks.

First, they are based on guiding the endmember extraction process to spatially large homogeneous areas expected to

Manuscript received August 21, 2012; revised October 17, 2012; accepted November 19, 2012. This work was supported in part by the Spanish Government under project DREAMS (TEC2011-28666-C04-04) and under project CEOS-SPAIN (AYA2011-29334-C02-02).

S. Lopez, J. F. Moure, G. M. Callico, J. F. Lopez, and R. Sarmiento are with the Institute for Applied Microelectronics (IUMA), Universidad de Las Palmas de Gran Canaria, 35017 Las Palmas de Gran Canaria, Spain (e-mail: seblopez@iuma.ulpgc.es; jfuentesmoure@gmail.com; gustavo@iuma.ulpgc.es; lopez@iuma.ulpgc.es; roberto@iuma.ulpgc.es).

A. Plaza is with the Hyperspectral Computing Laboratory, Department of Technology of Computers and Communications, University of Extremadura, 10003 Cáceres, Spain (e-mail: aplaza@unex.es).

Color versions of one or more of the figures in this paper are available online at http://ieeexplore.ieee.org.

Digital Object Identifier 10.1109/LGRS.2012.2229689

contain the purest signatures available in the scene. Although this strategy leads to obtaining a successful set of endmembers for many hyperspectral images, it also tends to obviate small targets or anomalous areas that may be present in the image. In addition, they may also guide the subsequent extraction algorithm to *homogenously mixed* areas, which do not contain pure pixels.

Second, when combined with computationally competitive endmember extraction approaches such as the vertex component analysis (VCA) algorithm [7], it results that the joint action of PP the image by means of the RBSPP or the SSPP algorithms and then extracting the endmembers from the resulting image takes more time than directly applying the VCA algorithm to the original nonpreprocessed image, which makes no sense from a computational point of view [5], [6]. This is mainly due to the computationally complex nature of the operations involved in the RBSPP and the SSPP algorithms, as well as to the fact that both PP stages tend to retain a significant amount of pixels from the original image.

Third, both algorithms show execution patterns that leave little room for introducing parallelism at the programming level, which is crucial for applications under real-time constraints. Moreover, the complex operations required by the RBSPP and the SSPP algorithms also demand a large amount of hardware resources when mapped onto dedicated hardware computing platforms, as it is the case of an hypothetical scenario of a satellite equipped with a hyperspectral imaging sensor, where linear unmixing could take place on board in order to reduce the delays in the delivery of Earth observation payload data to ground processing facilities.

In order to overcome the aforementioned limitations, this letter introduces a novel spatial–spectral PP module, which is based on selecting the pixels that are in the spatial edges (SEs) and in the spectral extremes (SEs) of the hyperspectral image under analysis. The proposed approach, called SE^{2}PP, solves the identified drawbacks while maintaining the same degree of accuracy than RBSPP and SSPP when coupled with traditional endmember extraction algorithms.

II. Review of Existing PP Approaches

This section briefly reviews previous approaches for SPP prior to endmember extraction, which will be used for quantitative validation and comparison with our newly developed approach.

The SPP [4] estimates, for each input pixel vector, a scalar factor that is intimately related to the spatial similarity between the pixel and its spatial neighbors and then uses this scalar factor to spatially weigh the spectral information associated to the pixel. The correction is performed so that pixels located in spatially homogeneous areas are expected to have a smaller displacement with regard to their original location in the data cloud than pure pixels surrounded by spectrally distinct substances. Resulting from the aforementioned operation, a modified simplex is formed, using not only spectral but also spatial information. The modified simplex serves as a guide for a subsequent competitive endmember identification process performed by any endmember extraction algorithm.

The RBSPP [5] also uses spatial information as a guide to exploit spectral information more effectively by adequately exploiting spatial context in adaptive fashion. This approach first adaptively searches for the most spectrally pure regions by using a hybrid procedure that combines unsupervised clustering and orthogonal subspace projection (OSP) concepts in order to find a set of spatially representative regions with associated spectra which are both spectrally pure and orthogonal between them. A standard endmember extraction algorithm is then applied to the pixels in the resulting spatially connected regions to produce the final endmembers.

The SSPP [6] first derives a spatial homogeneity index for each pixel in the hyperspectral image and performs unsupervised clustering to identify a set of clusters in spectral space. Finally, it fuses spatial and spectral information by selecting a subset of spatially homogeneous and spectrally pure pixels from each cluster. These pixels constitute the new set of candidates for endmember extraction.

III. Proposed SE^{2}PP Algorithm

This section introduces the SE^{2}PP algorithm proposed in this letter, whose ultimate goal is to select a subset of pixels from a given hyperspectral image that will be the input to a subsequent endmember extraction algorithm. The current section has been divided into three subsections: The first and second subsections are devoted to explain how these pixels are chosen from a spatial and a spectral points of view, respectively, while the third subsection details how both approaches are combined in the proposed SE^{2}PP algorithm.

A. Spatial Domain Analysis

The approaches in [2]–[6] are based on promoting the spatially homogeneous areas as the ones in which it is most likely to find pure pixels where, for the scope of this work, a spatially homogeneous area can be coarsely defined as a region of the image in which the dissimilarities between all its pixels are below a certain—and typically small—threshold.

One of the assumptions on which the SE^{2}PP algorithm is based is that, theoretically, and if no more information is provided, all the pixels enclosed in a region identified as a spatially homogeneous area have the same probability of becoming an endmember of the image. Moreover, in the surroundings of the frontier between two of these regions coexist pixels from both of them. Hence, if, rather than selecting a small amount of spatially large homogenous areas, a large amount of spatially small heterogeneous areas are selected at the PP level, the same extraction accuracy levels can be obtained while a fewer number of pixels are retained from the original image, as it will be demonstrated in the next section of this letter.

In order to identify these small heterogeneous areas located in the frontier between two spatially homogenous areas without incurring in an excessive computational cost, the following measurement of the *spatial activity (SA)* of a region of pixels is introduced:

$$\mathrm{SA} = \sum_{i=m_1}^{m_2} \sum_{j=n_1}^{n_2} |\boldsymbol{R}_{\mathbf{avg}}(\boldsymbol{i},\boldsymbol{j}) - \mu| \tag{2}$$

where R_{avg} represents an image that has the same pixels as R and only one spectral value per pixel obtained as the average of all the spectral bands of R (i.e., if R has P pixels of N

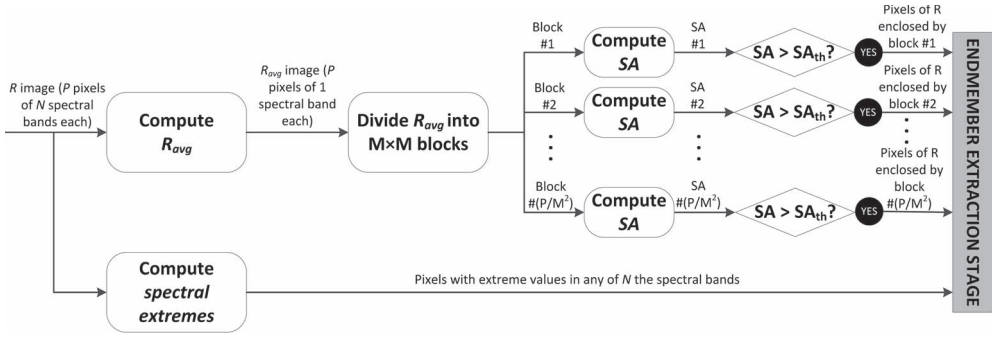

Fig. 1. Block diagram of the proposed SE^{2}PP algorithm.

spectral bands each as indicated in (1), then R_{avg} will have P pixels of one spectral value per pixel, which is obtained for each pixel as $r_{\mathrm{avg}} = ((r^1 + r^2 + \cdots + r^N)/N))$; (m_1, n_1) and (m_2, n_2) denote the absolute spatial coordinates of the region of the image being processed; and finally, μ represents the average value of all the pixels enclosed in the targeted region of the R_{avg} image.

From the definition mentioned earlier, it can be easily concluded that spatially homogenous areas will have low SA values, while on the contrary, heterogeneous areas will produce large values of the SA parameter.

B. Spectral Domain Analysis

Traditional endmember extraction algorithms, such as the NFINDR algorithm [8], operate in such a way that pixels with extreme values in any of the spectral bands of the sensed hyperspectral image are prone to be in the set of the final endmembers or, at least, prone to show a good match with one of them. Hence, the proposed SE^{2}PP algorithm takes advantage of this property by selecting, for each spectral band of R, only the 1% of the pixels that correspond with the highest values and the 1% of the pixels that correspond with the lowest values within each band of the image, following a similar strategy to the one recently disclosed in [9].

C. SE^{2}PP Algorithm

As it has been mentioned before, the proposed SE^{2}PP algorithm is based on selecting a reduced set of pixels from the original image in order to process only those pixels in a posterior endmember extraction stage. In order to do so, it first computes the R_{avg} image from the R image and then divides R_{avg} into nonoverlapped square blocks of pixels with the same spatial dimensions, which means that $(m_2 - m_1) = (n_2 - n_1) = M$. The SA of each of these blocks is further obtained, selecting only the pixels corresponding to blocks with a very high SA value, i.e., with a SA value above a predefined threshold $(\mathrm{SA_{th}})$, which has been defined in this work as follows:

$$\mathrm{SA_{th}} = M^2 \cdot \mu \cdot f \tag{3}$$

where f represents a scaling factor that modulates the amount of spatial heterogeneity associated to a block of pixels in order to be selected by the SE^{2}PP algorithm. In particular, we have set f to 0.05 because this was the value that empirically resulted in the best compromise between endmember extraction accuracy and speed for all the synthetic and real hyperspectral images that were tested in our experiments. In addition, the SE^{2}PP algorithm also selects those pixels in R that are identified as spectral extremes according to the procedure described in the previous subsection. Once this process is completed, the output (reduced) hyperspectral image provided by the SE^{2}PP algorithm is obtained by simply combining the pixels retained by both procedures, and those pixels are then transferred to the subsequent endmember extraction stage. For the sake of clarity, Fig. 1 provides a block diagram that summarizes the whole process carried out by the proposed SE^{2}PP PP stage.

Finally, it is important to highlight two main differences of the proposed SE^{2}PP algorithm with respect to the PP strategies described in [4]–[6]. First, all the operations involved in the SE^{2}PP algorithm are computationally simple which, as it will be demonstrated in the next section, enables SE^{2}PP to be much faster than its competitors. Moreover, all these operations can be easily implemented using a reduced amount of hardware resources, which is of crucial importance for real-time onboard systems. Second, the computations in the spatial domain are independent of the ones to be carried out in the spectral domain. Furthermore, in the spatial domain, the SA of each block of pixels can be computed independently from each other, while in the spectral domain, all the bands can be also independently processed. All these features clearly distinguish the proposed SE^{2}PP algorithm as a low cost, computationally simple, and highly parallelizable algorithm, undoubtedly attractive for onboard systems under real-time restrictions.

IV. Results

In this section, the performance of the proposed SE^{2}PP algorithm will be demonstrated. For this purpose, we have used a set of artificially generated hyperspectral images as well as the real well-known *Cuprite* hyperspectral image collected by the Airborne Visible/Infrared Imaging Spectrometer (AVIRIS).

A. Results Obtained With Synthetic Hyperspectral Images

The synthetic hyperspectral images used in this work were generated with the *Hyperspectral Imagery Synthesis toolbox for MATLAB* available at [10], which allowed us to create a hyperspectral image of a spatial size defined by the user from p spectral signatures selected from the U.S. Geological Survey (USGS) digital spectral library. In particular, we have utilized images of 400 × 400 pixels and 431 spectral bands each, which were generated with the default options given by the tool for generating abundances according to a Legendre distribution or to two different types of Gaussian functions (Matérn and Spheric). More concretely, we have generated three images

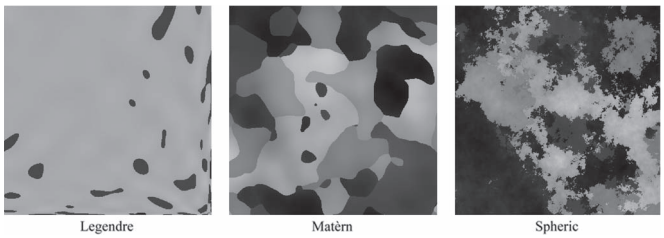

Fig. 2. Synthetic hyperspectral images generated with $p = 7$.

TABLE I
AVERAGE PROCESSING TIMES OBTAINED WITH ARTIFICIAL HYPERSPECTRAL IMAGES

Image	p	Algorithm	Average time (s)
Legendre	7	N-FINDR	121.22
		SE^{2}PP + NFINDR	6.31($M = 2$); 8.20 ($M = 4$)
	9	N-FINDR	141.96
		SE^{2}PP + NFINDR	5.44($M = 2$); 6.06($M = 4$)
	11	N-FINDR	121.79
		SE^{2}PP + NFINDR	8.23($M = 2$); 14.09($M = 4$)
Matérn	7	N-FINDR	85.69
		SE^{2}PP + NFINDR	10.51($M = 2$); 12.79($M = 4$)
	9	N-FINDR	102.78
		SE^{2}PP + NFINDR	10.22($M = 2$); 13.57($M = 4$)
	11	N-FINDR	103.10
		SE^{2}PP + NFINDR	14.40($M = 2$); 17.46($M = 4$)
Spheric	7	N-FINDR	98.08
		SE^{2}PP + NFINDR	17.96($M = 2$); 28.54($M = 4$)
	9	N-FINDR	99.08
		SE^{2}PP + NFINDR	16.84($M = 2$); 24.57($M = 4$)
	11	N-FINDR	106.94
		SE^{2}PP + NFINDR	22.14($M = 2$); 35.21($M = 4$)

for each type of function which correspond to three different values of p (7, 9, and 11). As it is observed in Fig. 2, where a snapshot of the images is depicted for the case of $p = 7$, the generated images have spatially homogenous areas as well as edges between them, as it is the case of the majority of real remotely sensed hyperspectral images.

Table I tabulates the average results obtained when running ten times per image the SE^{2}PP algorithm combined with the NFINDR (SE^{2}PP + NFINDR) with $M = 2$ and with $M = 4$ in a PC with Intel Quad Core CPU (at 3 GHz) and 4 GB of RAM memory. As far as the endmembers extracted in all the cases are perfectly matched with the ones computed by the NFINDR algorithm without any PP stage, only the results in terms of processing time have been reported. As it can be seen from Table I, the combination of the SE^{2}PP with the NFINDR algorithm is able to extract the same endmembers from the tested image but much faster than the NFINDR without a PP stage. Additionally, it is concluded that better processing times are obtained with $M = 2$ than with $M = 4$, which is completely logical as, in the second case, when a block of pixels is selected due to its associated SA value, 16 pixels are retained, while in the first case, only four pixels are retained per selected block.

B. Results Obtained With the Cuprite Data Set

In order to test the proposed SE^{2}PP algorithm in a more realistic scenario, the AVIRIS *Cuprite* image has also been used in this work. This scene is well understood mineralogically and has been widely used to validate the accuracy of endmember extraction algorithms. It consists of 350 $\times$ 350 pixels and 224 spectral bands between 0.4 and 2.5 μm. Prior to the analysis, different bands have been removed due to water absorption and low SNR resulting in a total of 188 spectral bands. In order to determine the number of endmembers of the image, the virtual dimensionality has been estimated by means of the noise-whitened Harsanyi–Farrand–Chang eigenthresholding method [11] using the Neyman–Pearson test with the false-alarm probability set to 10^{-5}, resulting in a total number of 19 different pure materials. This value is in agreement with the estimates provided by the well-known hyperspectral subspace identification method (HySime) [12].

For the case of *Cuprite* and with the purpose of validating the performance of our proposal in a more general way, the SE^{2}PP algorithm has been coupled not only to the NFINDR algorithm but also to the state-of-the-art OSP [13] and VCA endmember extraction algorithms. Fig. 3 shows (in white) the pixels of *Cuprite* selected by the SE^{2}PP algorithm with $M = 2$ (b) and with $M = 4$ (c) together with the original image (a), as well as the histograms of the SA values obtained for this image with $M = 2$ (d) and with $M = 4$ (e). As it can be seen from Fig. 3(d) and (e), the amount of blocks with large SA values is very small, and hence, the proposed SE^{2}PP algorithm retains a reduced amount of pixels from the original image [Fig. 3(b) and (c)]. In addition, Table II reports the average results obtained in terms of extraction accuracy, measured as the spectral angle scores (in degrees) obtained after comparing the USGS library spectra of *alunite* (A), *buddingtonite* (B), *calcite* (C), *kaolinite* (K), and *muscovite* (M) with the corresponding endmembers extracted by the different algorithms from the *Cuprite* scene, and in terms of processing time after 100 tests for $M = 2$ and for $M = 4$. As it can be observed from Table II, when the SE^{2}PP algorithm was combined with any of the three aforementioned endmember extraction algorithms, the achieved average accuracy was roughly the same than that without using a PP stage for both values of M. Nevertheless, in all the cases, the endmembers were extracted much faster when the proposed SE^{2}PP algorithm was taken into account, particularly for the case of $M = 2$. This is clearly inferred from the last column of Table II, where the speedup achieved for each test case has been displayed.

Table III provides a comparison of the proposed SE^{2}PP algorithm with respect to the other three state-of-the-art PP modules, namely, the SPP, RBSPP, and the SSPP algorithms. As it is observed, the proposed SE^{2}PP algorithm was able to obtain the same average levels of extraction accuracy than its predecessors while achieving much higher speedup factors. Furthermore, the SE^{2}PP algorithm was the only one that, when combined with the VCA algorithm, provided shorter processing times than the VCA algorithm by itself. Finally, the rightmost column of Table III reveals that our proposed approach is, by far, the most efficient, where a new measure of *endmember extraction efficiency (EEE)* has been defined for the scope of this work as follows:

$$\mathbf{EEE} = \frac{\mathbf{Speedup}}{\mathbf{Average\ spectral\ angle}} \cdot \mathbf{10}. \tag{4}$$

V. CONCLUSION

In this letter, a novel spatial–spectral PP algorithm called SE^{2}PP has been presented. The proposed method can be combined with existing endmember extraction algorithms (without modification of such algorithms) to produce solutions with

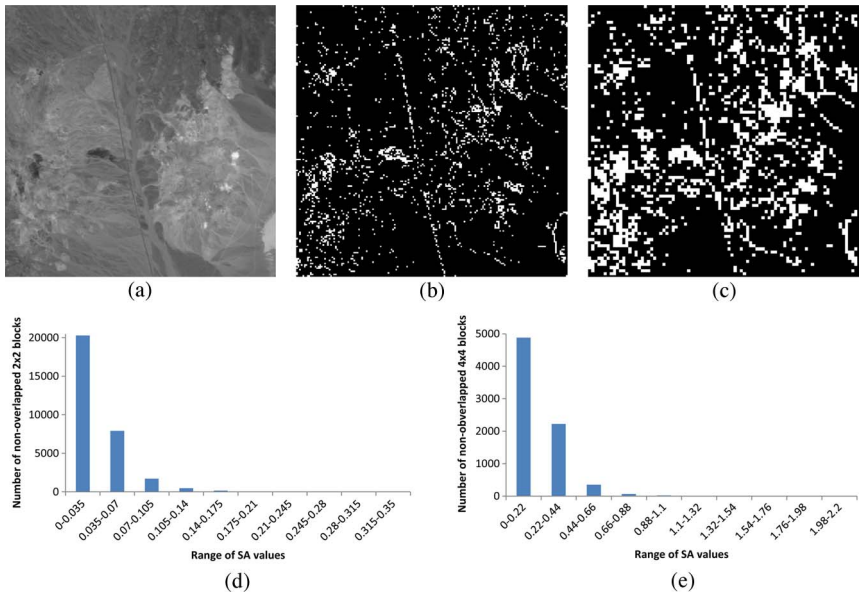

Fig. 3. Pixels of the (a) *Cuprite* image retained by the SE^{2}PP algorithm with (b) $M = 2$ and with (c) $M = 4$ together with the SA histograms obtained for (d) $M = 2$ and (e) $M = 4$.

TABLE II
SUMMARY OF THE RESULTS OBTAINED WITH THE CUPRITE DATA SET

Algorithm		Spectral angles (º)	Average spectral angle (º)	Average time (s)	Speedup
NFINDR		6.26 (A); 4.35 (B); 5.65 (C); 9.94 (K); 5.87 (M)	6.41	163.34	-
SE^{2}PP + NFINDR	$M = 2$	6.37 (A); 4.02 (B); 5.38 (C); 8.83 (K); 5.50 (M)	6.41	12.06	13.54
	$M = 4$	6.67 (A); 4.35 (B); 5.82 (C); 9.70 (K); 5.91 (M)	6.49	32.74	8.15
OSP		4.81 (A); 5.81 (B); 5.87 (C); 10.76 (K); 5.29 (M)	6.51	106.00	-
SE^{2}PP + OSP	$M = 2$	5.88 (A); 6.33 (B); 5.87 (C); 12.13 (K); 4.37 (M)	6.92	8.59	12.34
	$M = 4$	4.81 (A); 6.21 (B); 5.87 (C); 10.19 (K); 5.92 (M)	6.60	21.74	4.87
VCA		5.67 (A); 5.15 (B); 5.77 (C); 9.17 (K); 5.29 (M)	6.21	2.86	-
SE^{2}PP + VCA	$M = 2$	6.18 (A); 4.89 (B); 5.80 (C); 9.44 (K); 5.47 (M)	6.36	1.57	1.82
	$M = 4$	5.16 (A); 5.15 (B); 5.81 (C); 9.24 (K); 5.67 (M)	6.21	1.93	1.48

TABLE III
COMPARISON WITH STATE-OF-THE-ART APPROACHES

Algorithm		Average spectral angle (º)	Speedup	*EEE*
SPP+NFINDR		7.66	0.90	1.17
SPP+OSP		7.14	0.73	1.02
SPP+VCA		10.80	0.38	0.35
RBSPP+NFINDR		6.81	4.08	5.99
RBSPP+OSP		7.58	1.33	1.75
RBSPP+VCA		7.02	0.30	0.43
SSPP+NFINDR		6.60	5.02	7.61
SSPP+OSP		6.94	1.68	2.42
SSPP+VCA		7.52	0.39	0.52
SE^{2}PP+NFINDR	***M* = 2**	**6.41**	**13.54**	**21.12**
	***M* = 4**	**6.49**	**8.15**	**12.56**
SE^{2}PP+OSP	***M* = 2**	**6.92**	**12.34**	**17.83**
	***M* = 4**	**6.60**	**4.87**	**7.38**
SE^{2}PP+VCA	***M* = 2**	**6.36**	**1.82**	**2.86**
	***M* = 4**	**6.21**	**1.48**	**2.38**

reduced computational complexity while maintaining similar endmember identification accuracies. The results obtained with artificial and real hyperspectral images show that this PP method clearly outperforms other similar algorithms in terms of computational performance, obtaining similar average levels of extraction accuracy. Last but not least, the simplicity of the operations involved as well as their ease of parallelization validates the proposed SE^{2}PP algorithm for current and future hardware-based real-time onboard systems.

REFERENCES

[1] J. M. Bioucas-Dias, A. Plaza, N. Dobigeon, M. Parente, Q. Du, P. Gader, and J. Chanussot, "Hyperspectral unmixing overview: Geometrical, statistical and sparse regression-based approaches," *IEEE J. Sel. Topics Appl. Earth Observ. Remote Sens.*, vol. 5, no. 2, pp. 354–379, Apr. 2012.

[2] A. Plaza, P. Martinez, R. Perez, and J. Plaza, "Spatial/spectral endmember extraction by multidimensional morphological operations," *IEEE Trans. Geosci. Remote Sens.*, vol. 40, no. 9, pp. 2025–2041, Sep. 2002.

[3] D. M. Rogge, B. Rivard, J. Zhang, A. Sanchez, J. Harris, and J. Feng, "Integration of spatial–spectral information for the improved extraction of endmembers," *Remote Sens. Environ.*, vol. 110, no. 3, pp. 287–303, Oct. 2007.

[4] M. Zortea and A. Plaza, "Spatial preprocessing for endmember extraction," *IEEE Trans. Geosci. Remote Sens.*, vol. 47, no. 8, pp. 2679–2693, Aug. 2009.

[5] G. Martin and A. Plaza, "Region-based spatial preprocessing for endmember extraction and spectral unmixing," *IEEE Geosci. Remote Sens. Lett.*, vol. 8, no. 4, pp. 745–749, Jul. 2011.

[6] G. Martin and A. Plaza, "Spatial–spectral preprocessing prior to endmember identification and unmixing of remotely sensed hyperspectral data," *IEEE J. Sel. Topics Appl. Earth Observ. Remote Sens.*, vol. 5, no. 2, pp. 380–395, Apr. 2012.

[7] J. M. P. Nascimento and J. M. Bioucas-Dias, "Vertex component analysis: A fast algorithm to unmix hyperspectral data," *IEEE Trans. Geosci. Remote Sens.*, vol. 43, no. 4, pp. 898–910, Apr. 2005.

[8] M. E. Winter, "N-FINDR: An algorithm for fast autonomous spectral end-member determination in hyperspectral data," in *Proc. SPIE*, 1999, vol. 3753, pp. 266–275.

[9] J. Alves, J. Nascimento, J. Bioucas-Dias, V. Silva, and A. Plaza, "Parallel implementation of vertex component analysis for hyperspectral endmember extraction," in *Proc. IEEE IGARSS*, 2012, pp. 4078–4081.

[10] *Hyperspectral Imagery Synthesis Toolbox for MATLAB*. [Online]. Available: http://www.ehu.es/ccwintco/index.php/Hyperspectral_Imagery_Synthesis_tools_for_MATLAB

[11] C.-I. Chang and Q. Du, "Estimation of number of spectrally distinct signal sources in hyperspectral imagery," *IEEE Trans. Geosci. Remote Sens.*, vol. 42, no. 3, pp. 608–619, Mar. 2004.

[12] J. M. Bioucas-Dias and J. M. P. Nascimento, "Hyperspectral subspace identification," *IEEE Trans. Geosci. Remote Sens.*, vol. 46, no. 8, pp. 2435–2445, Aug. 2008.

[13] J. C. Harsanyi and C.-I. Chang, "Hyperspectral image classification and dimensionality reduction: An orthogonal subspace projection," *IEEE Trans. Geosci. Remote Sens.*, vol. 32, no. 4, pp. 779–785, Jul. 1994.